An extended finite element method (XFEM) for linear elastic fracture with smooth nodal stress

X. Peng [a], S. Kulasegaram [a], S.C. Wu [b], S.P.A. Bordas [a,c,d,*]

[a] Institute of Mechanics Materials and Advanced Manufacturing, Cardiff University, CF24 3AA, UK
[b] State Key Laboratory of Traction Power, Southwest Jiaotong University, Chengdu, 610031, China
[c] Université du Luxembourg, Faculté des Sciences, de la Technologie et de la Communication, 6 rue Richard Coudenhove-Kalergi, L-1359, Luxembourg
[d] Duy Tan University, 182 Nguyen Van Linh, Danang City, Vietnam

ARTICLE INFO

ABSTRACT

We present a method to achieve smooth nodal stresses in the XFEM. The salient feature of the method is to introduce an 'average' gradient into the construction of the approximation. Due to the higher-order polynomial basis provided by the interpolants, the new approximation enhances the smoothness of the solution without requiring an increased number of degrees of freedom. We conclude from numerical tests that the proposed method tends to be an efficient alternative to the classical XFEM, bypassing any postprocessing step to obtain smooth nodal stress fields and providing a direct means to compute local stress error measures.

1. Introduction

The extended finite element method (XFEM) [1] is a versatile approach to model strong discontinuities and singularities that exist in linear elastic fracture mechanics. In the XFEM, the approximation of the displacement field is decomposed into a regular part and an additional part (enriched part). The enriched part carries specific information or the solution such as discontinuity or singularity, through additional degrees of freedom (DOFs) associated with enriched nodes. The incorporation of enrichment functions into the approximation is based on the partition of unity method [2] and a more general version, named generalized FEM (GFEM) can be found in [3]. The XFEM provides great flexibility to model cracks since alignment of the mesh and cracks is unnecessary. The modeling procedure is simplified since the remeshing operations are no longer needed.

Apart from XFEM which broadly aims at providing approximations which are tailored to the solution, based on a priori knowledge about the solution, a number of interpolation methods have been developed in order to improve the efficiency of standard non-enriched FE methods. An example is the need for C^1 continu-

ous approximations, for instance, to solve problems where continuity of the first derivative of the unknown field is required. This is the case for higher-order gradient models, such as gradient elasticity [4], Kirchhoff-love shell models [5]. Fischer et al. [6] reviewed and compared the and the C^1 natural element method (NEM) with various C^1 finite elements. The C^1 NEM and FEM in their work are both based on Bernstein-Bezier representation. Some drawbacks of these elements such as mesh dependence, high computational cost and complex construction of isoparametric mesh are reported. Papanicolopulos and Zervos [7,8] created a series of triangular elements with C^1 continuous interpolation properties and they validated their methods by applications in strain-gradient elasticity. These C^1 elements looks promising while the extension to 3D is not reported yet. Various meshfree methods were introduced and also satisfy the need of C^1 continuity (to name a few [9–11]). The meshfree methods with or without enrichment have been applied to model complex 2D and 3D fracture problems [12–17], due to the flexibility in modeling fracture by point cloud instead of elemental mesh. Nevertheless, the construction of the shape functions of meshfree methods is computationally expensive, which hinders the application for complicated geometries.

Liu et al. proposed smoothed FEM (SFEM) by generalizing the strain smoothing technique. The SFEMs can be classified as node-based, edge-based and face-based smoothed FEM according to the form that the smoothing domains are associated. Researchers sub-

* Corresponding author at: Université du Luxembourg, Faculté des Sciences, de la Technologie et de la Communication, 6, rue Richard Coudenhove-Kalergi, L-1359, Luxembourg.

E-mail address: stephane.bordas@alum.northwestern.edu (S.P.A. Bordas).

sequently investigated the new methods to model fracture with or without partition of unity enrichment [18–22]. The extended SFEMs inherit the advantages of SFEMs and XFEM, and avoid evaluating singular integration on enriched elements due to the fact that only the basis functions, not the derivatives are needed in the integration, thus improving the convergence rate in XFEM without geometrical enrichment. To perform (extended) SFEMs, delicate element subdivision and renumbering need to be treated and more computational cost is brought by the increased bandwidth.

The goal of this work has been to construct simple approximations able to

- provide C^1 continuity almost everywhere;
- provide Kronecker delta property;
- rely on simplex meshes which are easily generated;
- be cheap to construct and integrate numerically;
- enable the treatment of propagating cracks with minimal remeshing.

This approximation procedure shares the attractive features of XFEM and higher-order continuous approximations. Two consecutive stages of interpolation are used in the construction of this approximation. The first stage of interpolation is performed by Lagrange interpolation to obtain nodal variables and nodal gradients. The problem field is reproduced in the latter interpolation using the nodal values and gradients derived from the previous interpolation. The re-constructed trial functions will maintain C^1 continuity at the nodes [23]. Cubic polynomials are contained in the space without increasing the total number of DOFs. This feature enhances the ability of the method to reproduce the solution near the crack tip [24] and improves the accuracy per DOF, The price to pay is increased computational expense per DOF, as discussed later in the paper. Particularly, essential differences are highlighted between the double-interpolation approximation and (extended) SFEMs, in which only standard basis functions are used for interpolation, then the smoothed strain can be obtained by a 'smoothing' operation on the constructed domain. While in the proposed work, new basis functions with C^1 continuity on nodes are obtained without element subdivision for the construction of smoothing domain. Analogous to meshfree methods, nodal stresses can be calculated in a straightforward manner without any post-processing.

The paper is organized as follows. In Section 2, the unenriched formulation for 1D and 2D is systematically introduced with a 1D bar example. Section 3 presents the discretized formulation of the enriched version of the proposed approximation for linear elastic fracture mechanics. Several numerical examples are presented to illustrate the advantages and limitations of the double-interpolation FEM (DFEM) and XFEM (XDFEM) in Section 4. Finally, in Section 5, concluding remarks are made with pointers to possible future work.

2. The double-interpolation approximation

2.1. 1D approximation by double-interpolation

The basic idea of the double-interpolation approximation is to interpolate the unknown fields, using both the primary nodal values and nodal gradients, which are generated by the finite element interpolation in simplex mesh discretization. The proposed 1D double-interpolation is comparable to Hermite interpolants. Fig. 1 shows a 1D domain which is discretized by five 1D elements. For the point of interest x in element e_3, the numerical value of the displacement can be interpolated by

$$\forall x \in [0, \ell], \quad u^h(x) = \phi_I(x)u^I + \psi_I(x)u^I_{,x} + \phi_J(x)u^J + \psi_J(x)u^J_{,x}, \tag{1}$$
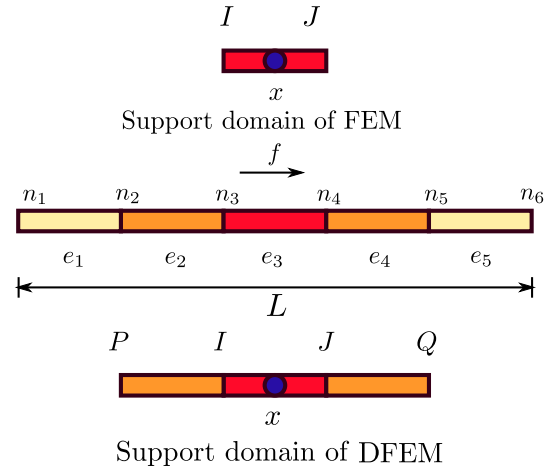

Fig. 1. Discretization of the 1D domain and the element support domain of FEM and DFEM.

where $u^I, u^I_{,x}$ denote the nodal displacement and nodal derivative of the displacement field at node I, respectively. $\ell = x_J - x_I$ is the length of the element. $\phi_I, \psi_I, \phi_J, \psi_J$ are the cubic Hermite basis polynomials given by:

$$\phi_I(x) = \left(1 + 2\left(\frac{x - x_I}{x_J - x_I}\right)\right)\left(\frac{x - x_J}{x_J - x_I}\right)^2, \tag{2a}$$

$$\psi_I(x) = (x - x_I)\left(\frac{x - x_J}{x_J - x_I}\right)^2, \tag{2b}$$

$$\phi_J(x) = \left(1 - 2\left(\frac{x - x_J}{x_J - x_I}\right)\right)\left(\frac{x - x_I}{x_J - x_I}\right)^2, \tag{2c}$$

$$\psi_J(x) = (x - x_J)\left(\frac{x - x_I}{x_J - x_I}\right)^2. \tag{2d}$$

We note that

$$\begin{aligned}
\phi_I(\mathbf{x}_L) &= \delta_{IL}, \quad \phi_{I,x}(\mathbf{x}_L) = 0, \\
\psi_I(\mathbf{x}_L) &= 0, \quad \psi_{I,x}(\mathbf{x}_L) = \delta_{IL},
\end{aligned} \tag{3}$$

which guarantees the Dirichlet boundary conditions can be exactly applied in the second stage of interpolation. If we define the local coordinates as follows,

$$L_I(x) = \frac{x - x_J}{\ell}, \quad L_J(x) = -\frac{x - x_I}{\ell}, \tag{4}$$

then the Hermite basis polynomials can be written as:

$$\phi_I(x) = L_I(x) + (L_I(x))^2 L_J(x) - L_I(x)(L_J(x))^2, \tag{5a}$$

$$\psi_I(x) = \ell L_J(x)(L_I(x))^2, \tag{5b}$$

$$\phi_J(x) = L_J(x) + (L_J(x))^2 L_I(x) - L_J(x)(L_I(x))^2, \tag{5c}$$

$$\psi_J(x) = -\ell L_I(x)(L_J(x))^2. \tag{5d}$$

Subsequently, we will use the 'average' nodal gradients $(\bar{u}^I_{,x}, \bar{u}^J_{,x})$ derived from finite element interpolation at each node to replace the gradients $(u^I_{,x}, u^J_{,x})$ in Eq. (1). But before we start calculating the average nodal gradients, an element set and a node set should be defined which closely relate to the derivation. First of all, we col-

lect all the elements contained in the support domain[1] for a point of interest into the element set Λ. Then, all the support nodes for a point of interest are listed in the node set $\mathcal{N}$. For instance, in Fig. 1, for the point of interest x inside element e_3, $\Lambda = \{e_3\}$ and $\mathcal{N} = \{n_3, n_4\}$ (or $\mathcal{N} = \{x_I, x_J\}$ in a local representation) for classical FEM. While for nodes on the element boundary, like n_3 (or x_I), $\Lambda_I = \{e_2, e_3\}$ and $\mathcal{N}_I = \{n_2, n_3, n_4\}$ (or $\mathcal{N}_I = \{x_P, x_I, x_J\}$) for classical FEM. Now Eq. (1) can be rewritten as:

$$u^h(x) = \phi_I(x)u^I + \psi_I(x)\bar{u}^I_{,x} + \phi_J(x)u^J + \psi_J(x)\bar{u}^J_{,x}, \tag{6}$$

where

$$u^I = u(x_I) = N^{e_3}_I(x_I)u^I + N^{e_3}_J(x_I)u^J, \tag{7}$$

$$\bar{u}^I_{,x} = \bar{u}_{,x}(x_I) = \omega_{e_2,I}u^{e_2}_{,x}(x_I) + \omega_{e_3,I}u^{e_3}_{,x}(x_I), \tag{8}$$

in which $N^{e_3}_I, N^{e_3}_J$ are linear finite element shape functions,[2] $u^{e_2}_{,x}(x_I)$ is the nodal derivative at x_I calculated in element e_2, which belongs to Λ_I, the support element set of x_I. $\omega_{e_2,I}$ denotes the weight of element e_2 in Λ_I. These parameters are calculated by:

$$u^{e_2}_{,x}(x_I) = N^{e_2}_{P,x}(x_I)u^P + N^{e_2}_{I,x}(x_I)u^I, \tag{9}$$

$$\omega_{e_2,I} = \frac{meas(e_{2,I})}{meas(e_{2,I}) + meas(e_{3,I})}, \tag{10}$$

where $N^{e_2}_{P,x}(x), N^{e_2}_{I,x}(x)$ are the derivatives of the corresponding shape functions associated with element e_2. $meas(\cdot)$ denotes the length of the 1D element. For the problem of elasticity, the nodal derivatives are the strains. One can find that the initial linear finite element approximation provides the strain field from each element (Eq. (9)), which will be used to obtain an averaged strain at each node (Eq. (8)). The obtained nodal average strain will be used in the re-construction of the approximation for displacement field by Hermite interpolation (Eq. (6)).

Substituting Eqs. (10) and (9), into Eq. (8) yields:

$$\begin{aligned}
\bar{u}^I_{,x} &= \bar{u}_{,x}(x_I) \\
&= \omega_{e_2,I}\left(N^{e_2}_{P,x}(x_I)u^P + N^{e_2}_{I,x}(x_I)u^I\right) \\
&\quad + \omega_{e_3,I}\left(N^{e_3}_{I,x}(x_I)u^I + N^{e_3}_{J,x}(x_I)u^J\right),
\end{aligned} \tag{11}$$

which can be rewritten as:

$$\bar{u}^I_{,x} = \begin{bmatrix} \omega_{e_2,I}N^{e_2}_{P,x} & \omega_{e_2,I}N^{e_2}_{I,x} + \omega_{e_3,I}N^{e_3}_{I,x} & \omega_{e_3,I}N^{e_3}_{J,x} \end{bmatrix}\begin{bmatrix} u^P \\ u^I \\ u^J \end{bmatrix}. \tag{12}$$

By defining,

$$\overline{N}_{L,x}(x_I) = \sum_{e_i \in \Lambda_I} \omega_{e_i,I}N^{e_i}_{L,x}(x_I), \quad L \in \mathcal{N}_I, \tag{13}$$

the averaged derivative at node x_I can be written as

$$\bar{u}^I_{,x} = \bar{u}_{,x}(x_I) = \overline{N}_{P,x}(x_I)u^P + \overline{N}_{I,x}(x_I)u^I + \overline{N}_{J,x}(x_I)u^J. \tag{14}$$

Now, substituting Eqs. (7) and (14) into (6) results in:

$$\begin{aligned}
u^h(x) &= \phi_I(x)\left(N_I(x_I)u^I + N_J(x_I)u^J\right) + \\
&\quad \psi_I(x)\left(\overline{N}_{P,x}(x_I)u^P + \overline{N}_{I,x}(x_I)u^I + \overline{N}_{J,x}(x_I)u^J\right) + \\
&\quad \phi_J(x)\left(N_I(x_J)u^I + N_J(x_J)u^J\right) + \\
&\quad \psi_J(x)\left(\overline{N}_{I,x}(x_J)u^I + \overline{N}_{J,x}(x_J)u^J + \overline{N}_{Q,x}(x_J)u^Q\right) \\
&= \psi_I(x)\overline{N}_{P,x}(x_I)u^P + \\
&\quad \left(\phi_I(x)N_I(x_I) + \psi_I(x)\overline{N}_{I,x}(x_I) + \phi_J(x)N_I(x_J) + \psi_J(x)\overline{N}_{I,x}(x_J)\right)u^I + \\
&\quad \left(\phi_I(x)N_J(x_I) + \psi_I(x)\overline{N}_{J,x}(x_I) + \phi_J(x)N_J(x_J) + \psi_J(x)\overline{N}_{J,x}(x_J)\right)u^J + \\
&\quad \psi_J(x)\overline{N}_{Q,x}(x_J)u^Q.
\end{aligned} \tag{15}$$

Hence, by defining,

$$\begin{aligned}
\widehat{N}_L(x) &= \phi_I(x)N_L(x_I) + \psi_I(x)\overline{N}_{L,x}(x_I) + \phi_J(x)N_L(x_J) \\
&\quad + \psi_J(x)\overline{N}_{L,x}(x_J),
\end{aligned} \tag{16}$$

the final form for the double-interpolation approximation can be obtained as:

$$u^h(x) = \sum_{L \in \widehat{\mathcal{N}}} \widehat{N}_L(x)u^L, \tag{17}$$

in which $\widehat{\mathcal{N}}$ denotes the support node set for the point of interest x in DFEM. We also use $\widehat{\Lambda}$ as the support element set in DFEM. Thus, for the point of interest x, $\widehat{\Lambda} = \Lambda_I \cup \Lambda_J = \{e_2, e_3, e_4\}$, $\widehat{\mathcal{N}} = \mathcal{N}_I \cup \mathcal{N}_J = \{n_2, n_3, n_4, n_5\}$ (or $\widehat{\mathcal{N}} = \{x_P, x_I, x_J, x_Q\}$ in the local representation as presented in Fig. 1). Due to the computation of $\bar{u}^I_{,x}$ and $\bar{u}^J_{,x}$, the support domain of point of interest x in e_3 has been expanded in the DFEM approximation. Similarly, the support domain of element boundary node n_3 (or x_I) is also larger in DFEM, i.e., $\widehat{\Lambda}_I = \{e_1, e_2, e_3, e_4\}$ and $\widehat{\mathcal{N}}_I = \{n_1, n_2, n_3, n_4, n_5\}$. It can be observed that derivative interpolants are embedded into Eq. (17). We can also infer that due to the enlargement of the local support domain, DFEM will result in an increased bandwidth, thus have an increased computational cost per DOF, but this is essential to construct the C^1 interpolants. Fig. 2 shows the DFEM shape function and derivative at node n_3.

To more clearly depict the behavior of the proposed method, a numerical example is considered in the following discussion. For this purpose a 1D bar of Young's modulus E, cross section A and length L (as illustrated in Fig. 1) problem is solved using both DFEM and FEM. The governing equations for the 1D problem are given by:

the equilibrium equation, $\quad EA\dfrac{d^2u}{dx^2} + f = 0$, $\tag{18a}$

the strain displacement relation, $\quad \epsilon(x) = u_{,x}(x)$, $\tag{18b}$

the constitutive law, $\quad \sigma(x) = E\epsilon_{,x}(x)$, $\tag{18c}$
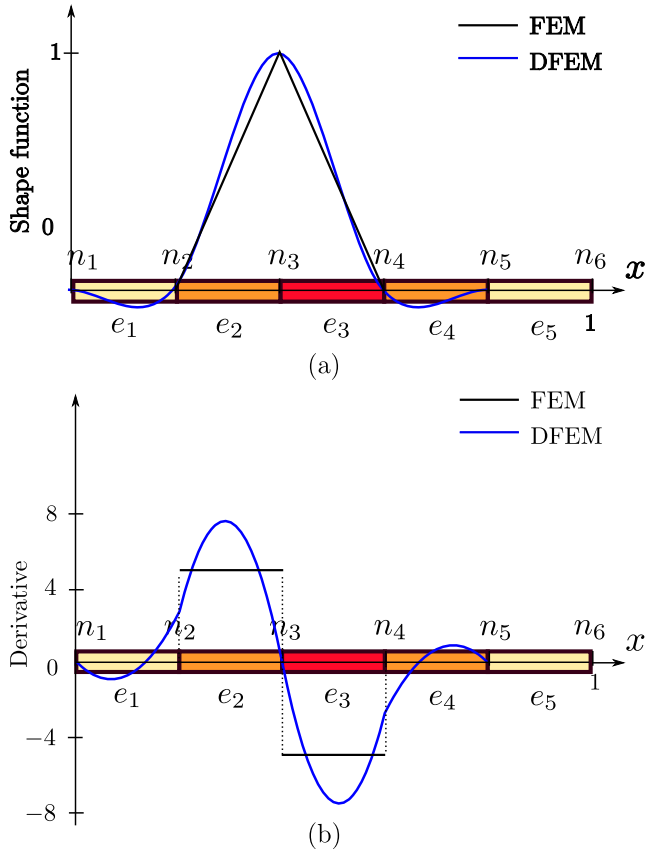
boundary condition, $\quad u|_{x=0} = 0, \text{and} \quad \sigma|_{x=L} = 0$, $\tag{18d}$

where f is a uniform body force applied to the 1D bar. The exact solution for the displacement and stress are given by:

$$u(x) = \frac{fL^2}{EA}\left(\frac{x}{L} - \frac{1}{2}\left(\frac{x}{L}\right)^2\right), \tag{19a}$$

$$\sigma(x) = \frac{fL}{A}\left(1 - \frac{x}{L}\right). \tag{19b}$$

For simplicity, all these parameters are assumed to have unit value in the simulation.

---

[1] Support domain means the region for a point of interest x in an element, where the shape functions are non-zero at x.

[2] In order to emphasis the support domain of FEM, the element number is used as the superscript of the shape functions. In Eq. (7), the displacement at x_I (or n_3) is interpolated in the element of interest e_3, although $N^{e_3}_J(x_I) = 0$, we still add this term for clarity.

Fig. 2. The 1D DFEM shape function and its derivative at node 3. Note that the shape functions do not satisfy the positivity condition, but do provide the Kronecker Delta property.

Fig. 3 compares the displacement and stress values obtained by both FEM and DFEM. It can be observed from the figure that DFEM captures the exact stress solution much better than FEM. The deterioration of the DFEM solution near the boundary nodes is attributed to the automatic recovery of the nodal gradients at the end points, which will be explained in the following section. Fig. 4 plots the relative error in the displacement and energy norm of the 1D bar problem (The definitions of these norms are given in Section 4). It is clearly illustrated that the DFEM approximation in 1D achieves at a rate comprised between the optimal rate of convergence for linear and quadratic complete approximation.

2.2. 2D approximation by double interpolation

As illustrated in Fig. 5, $\mathbf{x} = (x, y)$ denotes the point of interest in triangle IJK. Analogous to the derivation for the 1D formulation, the 2D double-interpolation approximation in a mesh of triangular element can be constructed as follows:

$$\mathbf{u}^h(\mathbf{x}) = \sum_{L \in \widehat{\mathcal{N}}} \widehat{N}_L(\mathbf{x}) \mathbf{u}^L, \tag{20}$$

$$\begin{aligned}
\widehat{N}_L(\mathbf{x}) = & \phi_I(\mathbf{x}) N_L(\mathbf{x}_I) + \psi_I(\mathbf{x}) \overline{N}_{L,x}(\mathbf{x}_I) + \varphi_I(\mathbf{x}) \overline{N}_{L,y}(\mathbf{x}_I) + \\
& \phi_J(\mathbf{x}) N_L(\mathbf{x}_J) + \psi_J(\mathbf{x}) \overline{N}_{L,x}(\mathbf{x}_J) + \varphi_J(\mathbf{x}) \overline{N}_{L,y}(\mathbf{x}_J) + \\
& \phi_K(\mathbf{x}) N_L(\mathbf{x}_K) + \psi_K(\mathbf{x}) \overline{N}_{L,x}(\mathbf{x}_K) + \varphi_K(\mathbf{x}) \overline{N}_{L,y}(\mathbf{x}_K),
\end{aligned} \tag{21}$$

where $\mathbf{u}^L$ is the nodal displacement vector. In the following discussion the evaluation of the average derivative of the shape function at node $\mathbf{x}_I$ is considered. The average derivative of the shape function at node $\mathbf{x}_I$ can be written as:
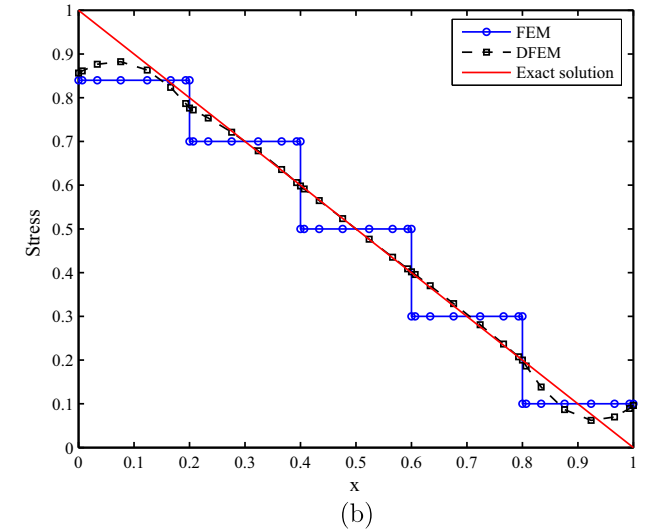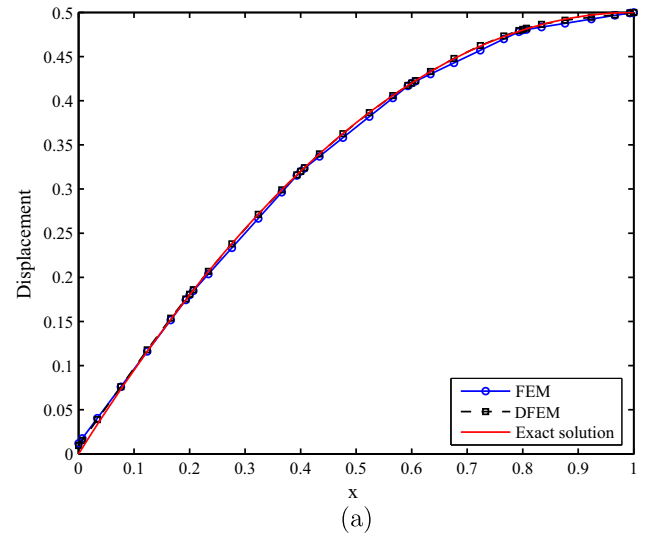
Fig. 3. The comparison of FEM and DFEM results for the 1D bar example: (a) displacement and (b) stress. Note that superior stress accuracy provided by DFEM.
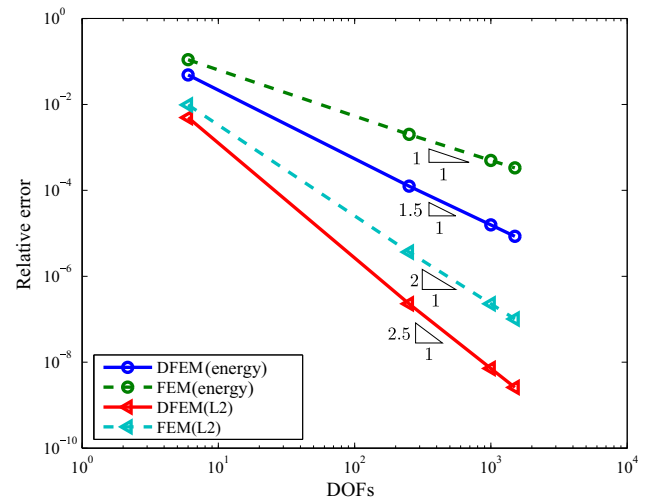
Fig. 4. Relative error in displacement and energy norm for the 1D bar problem.
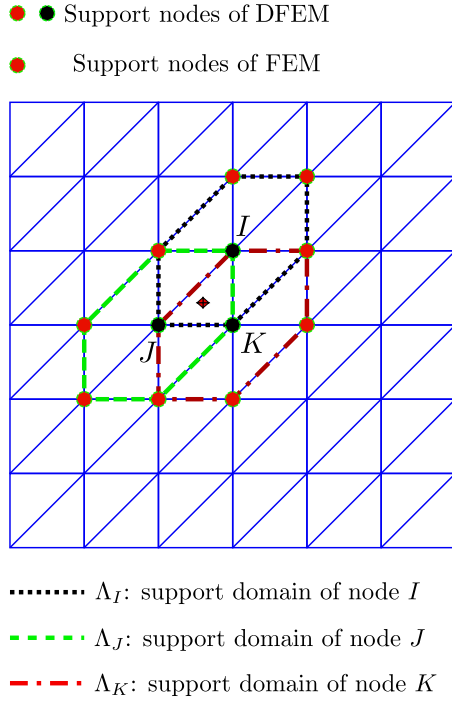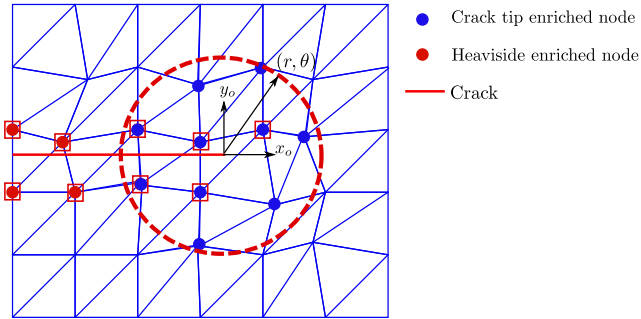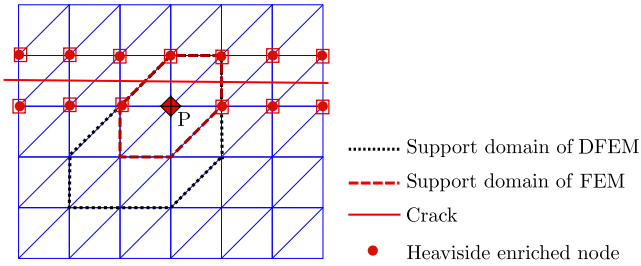
Fig. 5. Illustration for the support domain of DFEM.

Fig. 6. Nodal enrichment in XDFEM; the nodes encircled by red box are degenerated to C^0, see Section 2.3. (For interpretation of the references to colour in this figure legend, the reader is referred to the web version of this article.)

Fig. 7. The support domain of enriched DFEM; the nodes encircled by red box are degenerated to C^0, see Section 2.3. (For interpretation of the references to colour in this figure legend, the reader is referred to the web version of this article.)

$$\overline{N}_{L,x}(\mathbf{x}_I) = \sum_{e_{i,I} \in \Lambda_I} \omega_{e_{i,I}} N_{L,x}^{e_i}(\mathbf{x}_I), \tag{22a}$$

$$\overline{N}_{L,y}(\mathbf{x}_I) = \sum_{e_{i,I} \in \Lambda_I} \omega_{e_{i,I}} N_{L,y}^{e_i}(\mathbf{x}_I), \tag{22b}$$

where $\omega_{e_{i,I}}$ is the weight of element e_i in Λ_I and is computed by:

$$\omega_{e_{i,I}} = meas(e_i) \bigg/ \sum_{e_i \in \Lambda_I} meas(e_i). \tag{23}$$

Here $meas(\cdot)$ denotes the area of a triangular element. An example of how to evaluate the weight of an element is presented in Fig. 5. ϕ_I, ψ_I and φ_I form the polynomial basis associated with $\mathbf{x}_I$, which satisfies the following interpolating conditions:

$$\begin{aligned}
\phi_I(\mathbf{x}_L) &= \delta_{IL}, \quad \phi_{I,x}(\mathbf{x}_L) = 0, \quad \phi_{I,y}(\mathbf{x}_L) = 0, \\
\psi_I(\mathbf{x}_L) &= 0, \quad \psi_{I,x}(\mathbf{x}_L) = \delta_{IL}, \quad \psi_{I,y}(\mathbf{x}_L) = 0, \\
\varphi_I(\mathbf{x}_L) &= 0, \quad \varphi_{I,x}(\mathbf{x}_L) = 0, \quad \varphi_{I,y}(\mathbf{x}_L) = \delta_{IL}.
\end{aligned} \tag{24}$$

And these polynomial basis functions are given by:

$$\phi_I(\mathbf{x}) = L_I(\mathbf{x}) + (L_I(\mathbf{x}))^2 L_J(\mathbf{x}) + (L_I(\mathbf{x}))^2 L_K(\mathbf{x}) - L_I(\mathbf{x})(L_J(\mathbf{x}))^2 \\ - L_I(\mathbf{x})(L_K(\mathbf{x}))^2, \tag{25a}$$

$$\psi_I(\mathbf{x}) = -c_J\left(L_K(\mathbf{x})(L_I(\mathbf{x}))^2 + \frac{1}{2}L_I(\mathbf{x})L_J(\mathbf{x})L_K(\mathbf{x})\right) \\ + c_K\left((L_I(\mathbf{x}))^2 L_J(\mathbf{x}) + \frac{1}{2}L_I(\mathbf{x})L_J(\mathbf{x})L_K(\mathbf{x})\right), \tag{25b}$$

$$\varphi_I(\mathbf{x}) = b_J\left(L_K(\mathbf{x})(L_I(\mathbf{x}))^2 + \frac{1}{2}L_I(\mathbf{x})L_J(\mathbf{x})L_K(\mathbf{x})\right) \\ - b_K\left((L_I(\mathbf{x}))^2 L_J(\mathbf{x}) + \frac{1}{2}L_I(\mathbf{x})L_J(\mathbf{x})L_K(\mathbf{x})\right). \tag{25c}$$

Note that the polynomial basis functions $\phi_J, \psi_J, \varphi_J, \phi_K, \psi_K$ and φ_K can be obtained by the above definitions via cyclic permutation of indices I, J and K. In the above equations, L_I, L_J and L_K are the area coordinates of the point of interest $\mathbf{x}$ in triangle IJK. For the point of interest $\mathbf{x}$ in Fig. 5, the L_I, a_I, b_I and c_I are presented as follows:

$$L_I(\mathbf{x}) = \frac{1}{2meas(e_{IJK})}(a_I + b_I x + c_I y), \tag{26a}$$

$$a_I = x_J y_K - x_K y_J, \tag{26b}$$

$$b_I = y_J - y_K, \tag{26c}$$

$$c_I = x_K - x_J, \tag{26d}$$

Further, $L_J, L_K, a_J, b_J, b_K, a_I, c_J$ and c_K can be obtained using the above definitions via cyclic permutations of indices I, J and K (see Fig. 5).

When the point of interest lies on one of the edges, for example on edge IJ, the basis functions will boil down to 1D basis functions and will be consistent with the 1D form presented in the preceding section.

The DFEM shape functions possess the properties such as linear completeness, partition of unity and Kronecker delta property [23]. In addition, the 2D DFEM possesses C^1 continuity at the nodes and C^0 continuity on edges. Compared to 3-noded triangular elements, the DFEM basis functions can achieve a higher-order convergence rate without the introduction of additional nodes, which will be

seen the numerical examples in the next section. However, this attractive feature comes with the price of an increased bandwidth as the neighboring nodes are used to obtain the nodal gradients necessary for the second interpolation. The details of such computational costs will be discussed in the section devoted to numerical examples.

2.3. Modification of the nodal gradients

When C^0 continuity of the primal field at a node is needed, for instance on the nodes along a material interface, it is useful to modify the calculation of the average nodal gradient as discussed below. The calculation of the nodal gradient can be performed as follows:

$$\overline{N}_{L,x}(\mathbf{x}_I) = N^e_{L,x}(\mathbf{x}_I). \tag{27}$$

The right hand side is the derivative of N_L computed in element e, in which the point of interest $\mathbf{x}$ is located. This is easily done in the
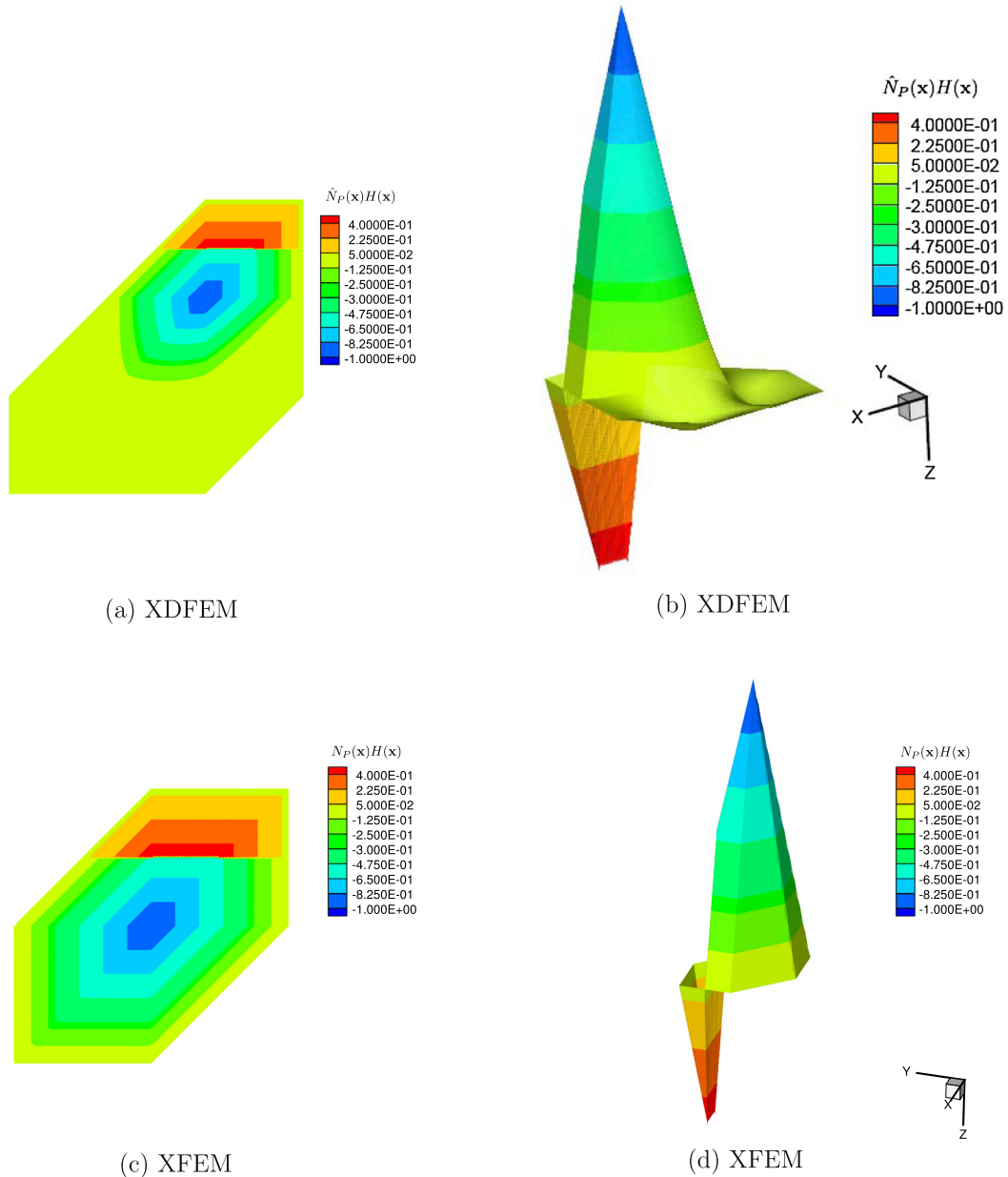

(a) XDFEM

(b) XDFEM

(c) XFEM

(d) XFEM

Fig. 8. Contour plot of Heaviside enriched shape functions.

implementation by replacing the average derivative with the derivative in the element of interest. It can be observed that nodes at the endpoint of a 1D bar automatically satisfy the above equation. All the Heaviside and topological enriched nodes in XFEM (the nodes circled by red boxes in Figs. 6 and 7) have been relaxed to C^0 as well due to the fact that during the calculation of average gradients in Eq. (22), the contribution from split elements cannot be computed directly as from continuous elements in an area weighted manner (Eq. (23)) due to the discontinuity. This is similar to difficulties encountered in smoothing enriched approximations [25,26].

2.4. The enriched 2D double-interpolation approximation

The XFEM for fracture has been the topic of substantial developments over past decades. Significant effort has been expended towards improving the accuracy and robustness of this method. In the standard XFEM, a local partition of unity is adopted, which means only certain nodes are enriched. This results in some elements (the blending elements) consisting of both regular and enriched nodes not fulfilling partition of unity. The existence of blending elements decreases accuracy and convergence rates. The enhanced strain method [27], the discontinuous Galerkin method [28] and other attempts [29,30] are investigated for this issue.

In terms of integration, the additional non-polynomial enrichment functions in the approximation space make the quadrature of the stiffness matrix of enriched elements and blending elements more delicate. Singularities, sharp gradients in the crack tip enrichment functions add to the complexity of numerical integration. The traditional procedure to perform the integration is to subdivide the enriched elements and blending elements into quadrature subcells [1]. Many efforts have been done like substitution of the non-polyniamls by 'equivalent' polynomials [31], the Schwarz-Christoffel mapping of the polygonal elements cut by the crack [32] and the almost polar integration within crack tip enriched elements [33]. Another efficient integration scheme was transforming the domain integration into contour integration in [30,18].

The crack can be described in XFEM by enriching the standard displacement approximation as follows:

$$\mathbf{u}^h(\mathbf{x}) = \sum_{I \in \mathcal{N}_I} \widehat{N}_I(\mathbf{x}) \mathbf{u}^I + \sum_{J \in \mathcal{N}_J} \widehat{N}_J(\mathbf{x}) H(\mathbf{x}) \mathbf{a}^J$$
$$+ \sum_{K \in \mathcal{N}_K} \widehat{N}_K(\mathbf{x}) \sum_{\alpha=1}^{4} f_\alpha(\mathbf{x}) \mathbf{b}^{K\alpha}, \tag{28}$$

where $\mathbf{u}^I$ are the regular DOFs, $\mathbf{a}^J$ are the additional Heaviside enriched DOFs, and $\mathbf{b}^{K\alpha}$ are the additional crack tip enriched DOFs. $\mathcal{N}_I, \mathcal{N}_J$ and $\mathcal{N}_K$ are the collections of regular non-enriched nodes, Heaviside enriched nodes and crack tip enriched nodes, respectively. $H(\cdot)$ is the Heaviside function. The crack tip enrichment functions are defined as:

$$\left\{ f_\alpha(r,\theta), \alpha=1,4 \right\} = \left\{ \sqrt{r}\sin\frac{\theta}{2}, \sqrt{r}\cos\frac{\theta}{2}, \sqrt{r}\sin\frac{\theta}{2}\sin\theta, \sqrt{r}\cos\frac{\theta}{2}\sin\theta \right\}, \tag{29}$$

where (r, θ) are the polar coordinates of the crack tip (Fig. 6). Fig. 8 compares the Heaviside enriched shape functions obtained with XFEM and XDFEM which are defined in Fig. 7.

3. Weak form and discretized formulations

For an elastic body as in Fig. 9 defined by Hooke's tensor $\mathbf{C}$ and undergoing small strains and small displacements, the equilibrium equations and boundary conditions for the Cauchy stress $\boldsymbol{\sigma}$ and the displacement field $\mathbf{u}$ write:

$$\begin{aligned} \nabla \cdot \boldsymbol{\sigma} &= \mathbf{0} && \text{in} && \Omega, \\ \boldsymbol{\sigma} \cdot \mathbf{n} &= \bar{\mathbf{t}} && \text{on} && \Gamma_t, \\ \mathbf{u} &= \bar{\mathbf{u}} && \text{on} && \Gamma_u. \end{aligned} \tag{30}$$

Here $\bar{\mathbf{t}}$ is the traction imposed on boundary Γ_t. Further, assuming traction free crack faces:

$$\boldsymbol{\sigma} \cdot \mathbf{n} = \mathbf{0} \qquad \text{on} \quad \Gamma_{c^+} \quad \text{and} \quad \Gamma_{c^-}, \tag{31}$$

where $\Gamma_{c^+}, \Gamma_{c^-}$ are the upper and lower crack surfaces respectively. The strain-displacement relation and the constitutive law are respectively as:

$$\boldsymbol{\epsilon} = \frac{1}{2} \left(\nabla + \nabla^{\mathrm{T}} \right) \otimes \mathbf{u}, \tag{32a}$$

$$\boldsymbol{\sigma} = \mathbf{C} : \boldsymbol{\epsilon}. \tag{32b}$$
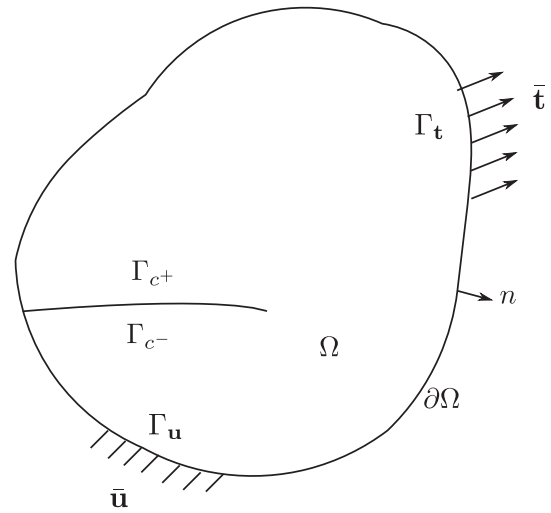
Fig. 9. Elastic body with a crack, $\partial\Omega = \Gamma_{\mathbf{u}} \cup \Gamma_{\mathbf{t}}, \Gamma_{\mathbf{u}} \cap \Gamma_{\mathbf{t}} = \varnothing$.
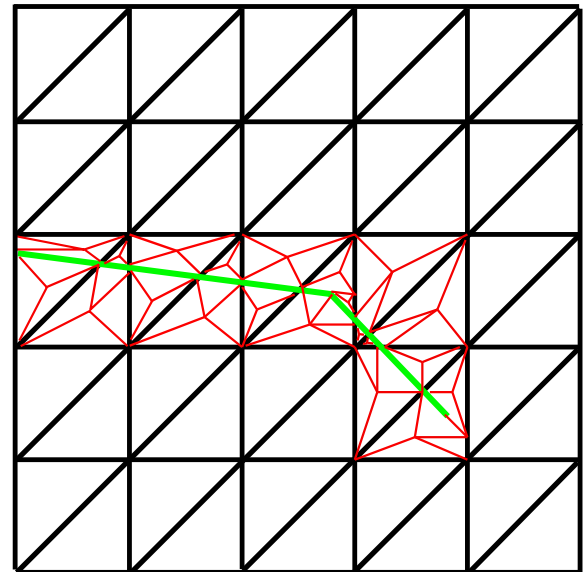

Fig. 10. Elements subdivision for quadrature in XFEM and XDFEM.

Using a Bubnov-Galerkin weighted residual formulation based on Lagrange test and trial spaces, substituting the trial and test functions into the weak form of Eq. (30), and using the arbitrariness of nodal variations, the discretized equations can be written:

$$\mathbf{Ku} = \mathbf{f}, \tag{33}$$

where $\mathbf{u}$ is the nodal vector of the unknown displacements and $\mathbf{K}$ is the stiffness matrix. The elemental form of $\mathbf{K}$ for element e is given by:

$$\mathbf{K}_{IJ}^{e} = \begin{bmatrix} \mathbf{K}_{IJ}^{uu} & \mathbf{K}_{IJ}^{ua} & \mathbf{K}_{IJ}^{ub} \\ \mathbf{K}_{IJ}^{au} & \mathbf{K}_{IJ}^{aa} & \mathbf{K}_{IJ}^{ab} \\ \mathbf{K}_{IJ}^{bu} & \mathbf{K}_{IJ}^{ba} & \mathbf{K}_{IJ}^{bb} \end{bmatrix}. \tag{34}$$

The external force vector $\mathbf{f}$ is defined as

$$\mathbf{f}_I = \{\mathbf{f}_I^u \quad \mathbf{f}_I^a \quad \mathbf{f}_I^{b^1} \quad \mathbf{f}_I^{b^2} \quad \mathbf{f}_I^{b^3} \quad \mathbf{f}_I^{b^4}\}. \tag{35}$$

The submatrices and vectors in Eqs. (34) and (35) are:

$$\mathbf{K}_{IJ}^{rs} = \int_{\Omega^e} (\mathbf{B}_I^r)^T \mathbf{C} \mathbf{B}_J^s d\Omega \qquad (r, s = u, a, b), \tag{36a}$$

$$\mathbf{f}_I^u = \int_{\partial\Omega_t^h \cap \partial\Omega^e} \widehat{N}_I \bar{\mathbf{t}} d\Gamma, \tag{36b}$$

$$\mathbf{f}_I^a = \int_{\partial\Omega_t^h \cap \partial\Omega^e} \widehat{N}_I H \bar{\mathbf{t}} d\Gamma, \tag{36c}$$

$$\mathbf{f}_I^{b^\alpha} = \int_{\partial\Omega_t^h \cap \partial\Omega^e} \widehat{N}_I f_\alpha \bar{\mathbf{t}} d\Gamma \qquad (\alpha = 1, 2, 3, 4). \tag{36d}$$

In Eq. (36a), $\mathbf{B}_I^u, \mathbf{B}_I^a$ and $\mathbf{B}_I^{b^\alpha}$ are given by

$$\mathbf{B}_I^u = \begin{bmatrix} \widehat{N}_{I,x} & 0 \\ 0 & \widehat{N}_{I,y} \\ \widehat{N}_{I,y} & \widehat{N}_{I,x} \end{bmatrix}, \tag{37a}$$

$$\mathbf{B}_I^a = \begin{bmatrix} (\widehat{N}_I(H - H_I))_{,x} & 0 \\ 0 & (\widehat{N}_I(H - H_I))_{,y} \\ (\widehat{N}_I(H - H_I))_{,y} & (\widehat{N}_I(H - H_I))_{,x} \end{bmatrix}, \tag{37b}$$

$$\mathbf{B}_I^b = \begin{bmatrix} \mathbf{B}_I^{b^1} & \mathbf{B}_I^{b^2} & \mathbf{B}_I^{b^3} & \mathbf{B}_I^{b^4} \end{bmatrix}, \tag{37c}$$

$$\mathbf{B}_I^{b^\alpha} = \begin{bmatrix} (\widehat{N}_I(f_\alpha - f_{\alpha I}))_{,x} & 0 \\ 0 & (\widehat{N}_I(f_\alpha - f_{\alpha I}))_{,y} \\ (\widehat{N}_I(f_\alpha - f_{\alpha I}))_{,y} & (\widehat{N}_I(f_\alpha - f_{\alpha I}))_{,x} \end{bmatrix} \qquad (\alpha = 1 - 4). \tag{37d}$$

In order to obtain the nodal displacements in a more straightforward manner, the shifted-basis is adopted in the above equations. More details regarding XFEM implementation can be found in [34].

The strategies of numerical integration for XDFEM is similar to standard XFEM. A simple subdivision for Heaviside enriched elements and tip enriched elements is performed for quadrature as in Fig. 10. Due to the introduction of higher-order polynomials in the basis functions of XDFEM, 4 Gauss points are adopted for each regular element whilst only 1 Gauss point in standard XFEM. And the Gauss quadrature is outlined briefly as.

- regular elements: 1 Gauss point in XFEM and 4 Gauss points in XDFEM;
- Heaviside enriched elements: 1 Gauss point for each sub-cell in XFEM and 4 Gauss points for each sub-cell in XDFEM;
- Tip blending elements: 7 Gauss points for each element in both XFEM and XDFEM;
- Tip enriched elements: 16 Gauss points for each sub-cell in both XFEM and XDFEM;

4. Numerical examples

A set of numerical examples is chosen to assess the efficiency and usefulness of the double-interpolation and its enriched form. In order to assess the convergence rate of each method, the relative error measured in the displacement L_2 norm and the energy norm are defined, respectively, as:

$$R_d = \sqrt{\frac{\int_\Omega (\mathbf{u}^h - \mathbf{u})^T (\mathbf{u}^h - \mathbf{u}) d\Omega}{\int_\Omega \mathbf{u}^T \mathbf{u} d\Omega}}, \tag{38a}$$

$$R_e = \sqrt{\frac{\int_\Omega (\boldsymbol{\sigma}^h - \boldsymbol{\sigma})^T (\boldsymbol{\epsilon}^h - \boldsymbol{\epsilon}) d\Omega}{\int_\Omega \boldsymbol{\sigma}^T \boldsymbol{\epsilon} d\Omega}}. \tag{38b}$$

where the fields with superscript 'h' refer to the approximation, and $\boldsymbol{\sigma}, \boldsymbol{\epsilon}, \mathbf{u}$ are exact fields. Unless specified otherwise, the *Young's modulus E* and *Poisson's ratio ν* are assumed to be 1000 and 0.3 respectively. The constants μ and κ are given by:
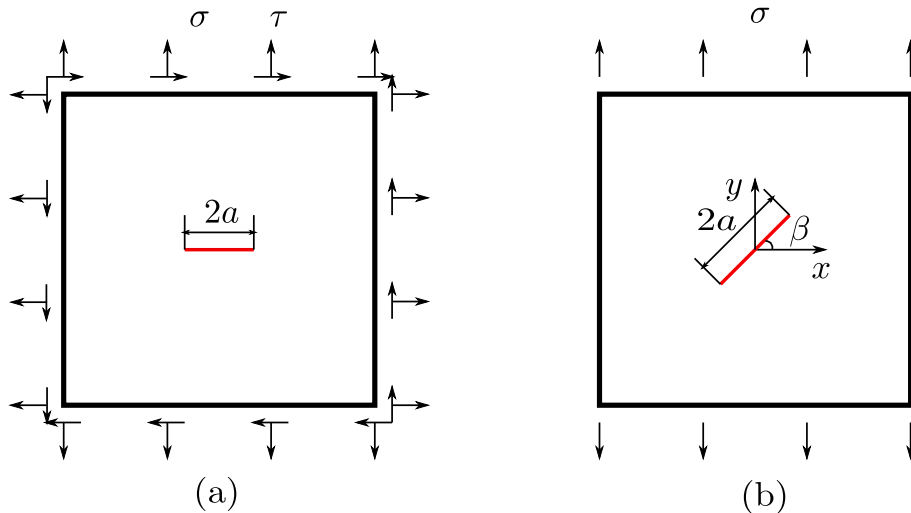

Fig. 11. (a) Griffith crack and (b) inclined crack.

$$\mu = \frac{E}{2(1+v)}, \tag{39a}$$

$$\kappa = \begin{cases} 3 - 4v, & \text{Plane strain} \\ (1-v)/(3+v), & \text{Plane stress} \end{cases}$$

4.1. Griffith crack

A Griffith crack problem is shown in Fig. 11(a). An infinite plate with a crack segment ($a = 5.$) subjected to remote tensile loads is considered here. A square domain (10×10) encircling the crack tip is selected and the analytical displacement is applied on the boundary. The domain is discretized respectively by $11 \times 11, 47 \times 47, 111 \times 111, 201 \times 201, 351 \times 351$ and 701×701 structured meshes. The maximum DOF is about 1 million. The analytical displacement and stress fields are given by [35]:
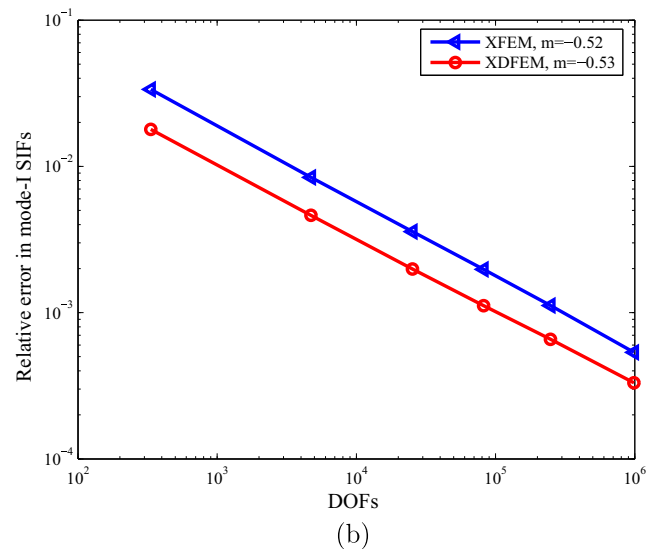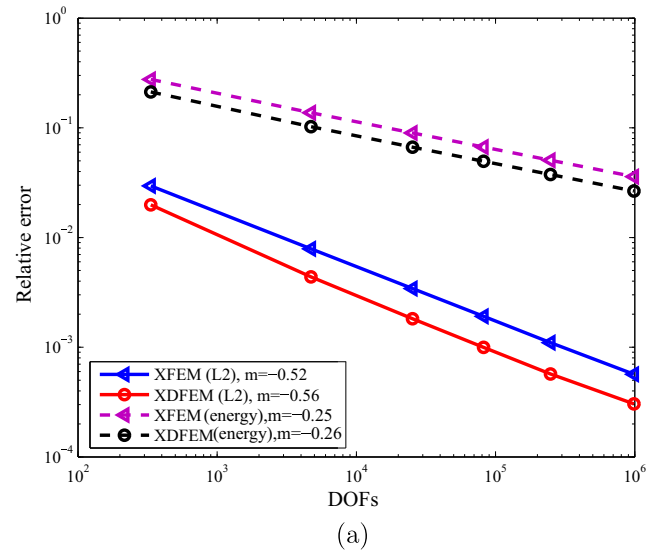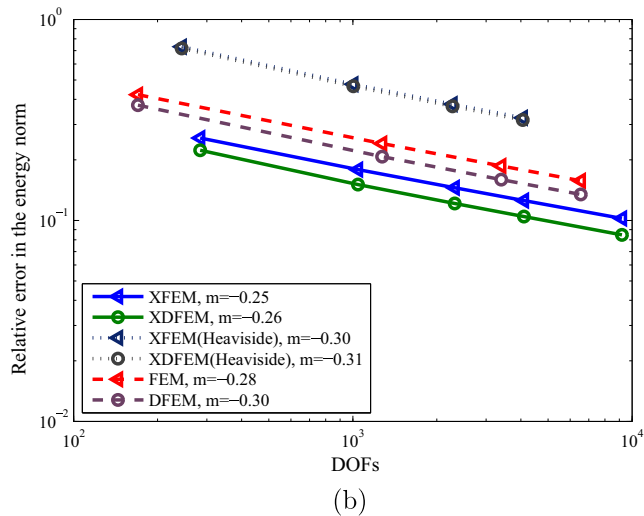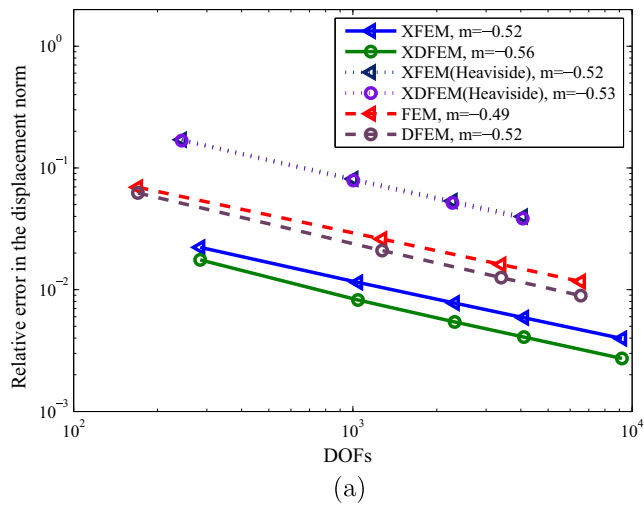
$$\sigma_{xx}(r,\theta) = \frac{K_I}{\sqrt{2\pi r}} \cos\frac{\theta}{2}\left(1 - \sin\frac{\theta}{2}\sin\frac{3\theta}{2}\right) \\ - \frac{K_{II}}{\sqrt{2\pi r}}\sin\frac{\theta}{2}\left(2 + \cos\frac{\theta}{2}\cos\frac{3\theta}{2}\right), \tag{40a}$$

$$\sigma_{yy}(r,\theta) = \frac{K_I}{\sqrt{2\pi r}}\cos\frac{\theta}{2}\left(1 + \sin\frac{\theta}{2}\sin\frac{3\theta}{2}\right) \\ + \frac{K_{II}}{\sqrt{2\pi r}}\sin\frac{\theta}{2}\cos\frac{\theta}{2}\cos\frac{3\theta}{2}, \tag{40b}$$

$$\tau_{xy}(r,\theta) = \frac{K_I}{\sqrt{2\pi r}}\sin\frac{\theta}{2}\cos\frac{\theta}{2}\cos\frac{3\theta}{2} \\ + \frac{K_{II}}{\sqrt{2\pi r}}\cos\frac{\theta}{2}\left(1 - \sin\frac{\theta}{2}\sin\frac{3\theta}{2}\right), \tag{40c}$$

$$u_x(r,\theta) = \frac{K_I}{2\mu}\sqrt{\frac{r}{2\pi}}\cos\frac{\theta}{2}\left(\kappa - 1 + 2\sin^2\frac{\theta}{2}\right) \\ + \frac{(1+v)K_{II}}{E}\sqrt{\frac{r}{2\pi}}\sin\frac{\theta}{2}\left(\kappa + 1 + 2\cos^2\frac{\theta}{2}\right), \tag{40d}$$

$$u_y(r,\theta) = \frac{K_I}{2\mu}\sqrt{\frac{r}{2\pi}}\sin\frac{\theta}{2}\left(\kappa + 1 - 2\cos^2\frac{\theta}{2}\right) \\ + \frac{(1+v)K_{II}}{E}\sqrt{\frac{r}{2\pi}}\cos\frac{\theta}{2}\left(1 - \kappa + 2\sin^2\frac{\theta}{2}\right), \tag{40e}$$

Fig. 12. Relative error in the displacement and energy norm of in Griffith crack for explicit crack representation (dashed lines), Heaviside enrichment only (dotted lines) and topological enrichment (solid lines).
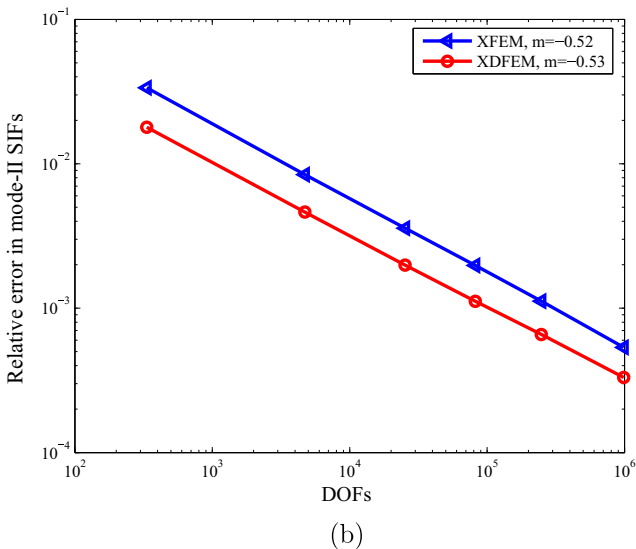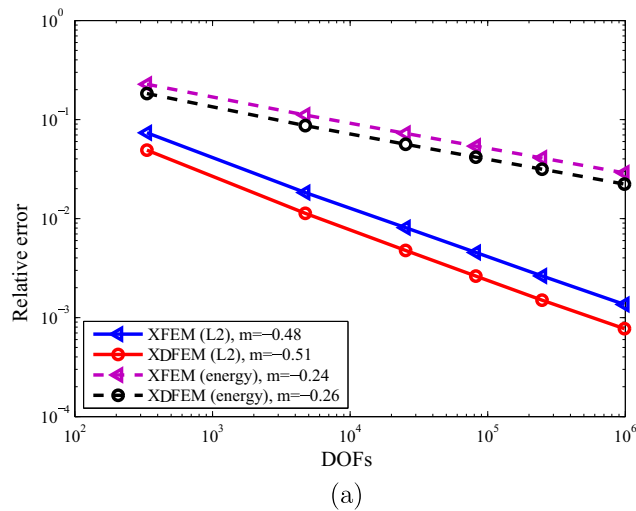

Fig. 13. Convergence results of Griffith crack (mode-I) for topological enrichment: (a) the error in the displacement L_2 and energy norm and (b) the error in SIFs.

where K_I and K_{II} are the stress intensity factors (SIFs) for mode-I and mode-II, respectively. (r, θ) are the polar coordinates used to define the crack geometry.

4.1.1. Convergence study

The Griffith crack problem is first used to investigate the enrichment effects of DFEM. The convergence rate in XDFEM is studied in three ways: explicit crack representation (where the crack is explicitly meshed), Heaviside enrichment only and full Heaviside and asymptotic enrichment. These results are plotted in Fig. 12. From Fig. 12, it can be concluded that the DFEM yields better accuracy and slightly improves the convergence rate compared to FEM for all the cases considered. It also transpires from the results that the full enrichment of DFEM produces better accuracy than modeling the crack explicitly. Note that we make no correction for blending issues in partially enriched elements [27].

1 million DOF problems in both mode-I and mode-II were simulated to assess the convergence rate of the method (see Figs. 13 and 14). The relative errors in the SIFs are also shown in the plots. We study the case where only tip enrichment is used, which is known [33,36] to lead to the same convergence rate as the standard Lagrange-based FEM, and which is confirmed here also for XDFEM, as expected.

We also observe that XDFEM is, as XFEM, able to reproduce the discontinuity across the crack faces. When geometrical enrichment with an enrichment radius of 1/5 of the crack length is used (Fig. 15), optimality is recovered and the XDFEM solution is also more accurate than the XFEM solution in terms of displacement, energy and SIFs. Fig. 16 illustrates the number of iterations required for the Conjugate Gradient (CG) solver to converge, which can be regarded as an indication to the condition number of the stiffness matrix. It is observed that XDFEM performs slightly worse than XFEM in terms of the condition number. As expected, when a fixed area enrichment is used, the deterioration of the condition number is accentuated compared to the case when only the element containing the tip is enriched. These conclusions are in agreement with the investigation reported in [33,37].

4.1.2. Accuracy study

Though it was already established from the convergence curves that over the whole computational domain, the XDFEM is generally slightly more accurate than XFEM for a given number of DOFs, it is necessary in practice to investigate whether XDFEM improves the precision also locally in the vicinity of the crack tip. The strain component ϵ_{yy} is plotted along the line perpendicular to the crack in
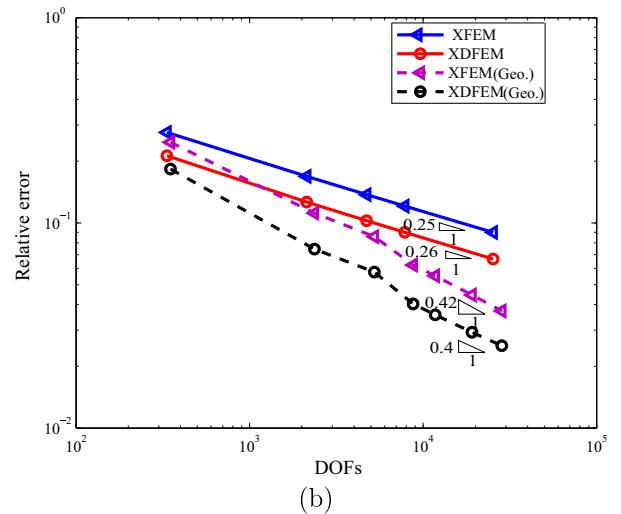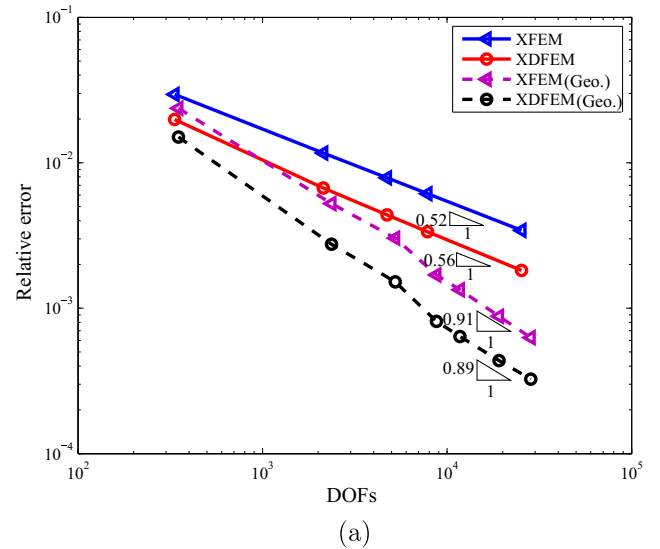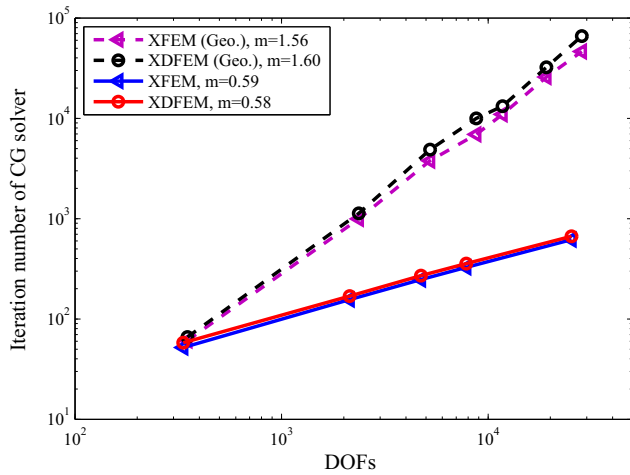

(a)

(a)

(b)

(b)

Fig. 14. Convergence results of Griffith crack (mode-II) for topological enrichment: (a) the error in the displacement L_2 and energy norm and (b) the error in SIFs.

Fig. 15. Convergence results of topological enrichment (solid lines) and geometrical enrichment (Geo., dashed lines) for mode-I: (a) the error in the displacement L_2 norm and (b) the error in the energy norm.

Fig. 16. Iteration number of CG solver; solid lines for topological enrichment, dashed lines for geometrical enrichment.
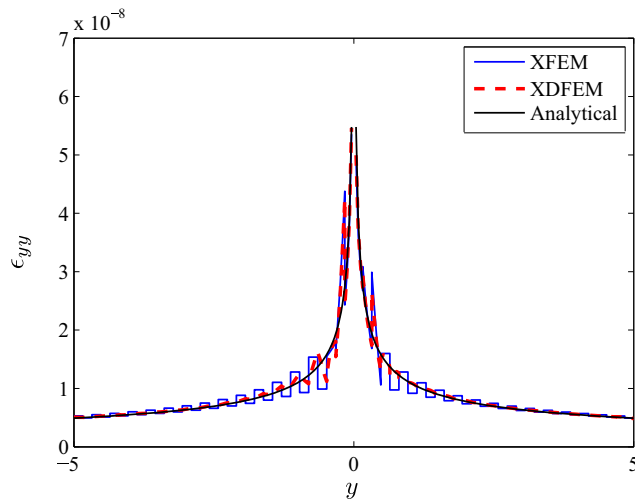
Fig. 17. The comparison of the strain component along line $x = 0$.

front of the tip (the line $x = 0$) in a 31×31 structured mesh in Fig. 17. It can be observed that in the vicinity of the crack tip, both XFEM and XDFEM will show drastic oscillation in the ϵ_{yy}, due to the introduced trigonometric branch enrichment function. From Fig. 17, we can conclude that the XDFEM result is much closer to the analytical solution than that of XFEM in the far field of the crack tip and reduce the oscillation in the vicinity of the crack tip, thanks to the inclusion of nodal gradients in the approximation.

The mesh distortion effect is also investigated in this example. A structured mesh and typical distorted mesh are shown in Fig. 18. The results are listed in Table 1. The precision of XDFEM in distorted mesh appears to be superior to that of the XFEM, although this superiority is mild.

4.1.3. Computational efficiency

It should be highlighted that the support domain of DFEM element is much bigger than that of FEM element due to the introduction of the nodal gradient into the approximation (see Figs. 1 and 5). This directly results in increased bandwidth of the stiffness matrix in DFEM. Consequently, the computational time per DOFs is expected to be larger for DFEM than for the FEM. Figs. 19 and 20(a) show the comparison of the time cost in assembling the stiffness matrix, solving the linear equations and the total time of the two processes. It can be seen that with the model size increasing, XDFEM requires less time to obtain the same precision. For the solution process, XFEM produces an error 1.4 times higher ($\frac{XFEM15.48}{XDFEM11.} = 1.4$) than the XDFEM at the same computational time of 0.06 s. The total time comparison shows that after $t_0 = 0.6$ s, XDFEM is more efficient computationally than XFEM in terms of the energy error. It can be observed from Fig. 20(b) that XDFEM is always superior to XFEM in the same DOFs. The main cause of

Table 1
Relative error in the energy norm for regular structured meshes and distorted meshes.

DOFs	Structured mesh		distorted mesh	
	XFEM	XDFEM	XFEM	XDFEM
334	0.2272	0.1832	0.2313	0.1882
4726	0.1112	0.08672	0.1132	0.08863
7834	0.09769	0.07600	0.1016	0.08261
17134	0.08006	0.06212	0.08223	0.06215

(a)   (b)
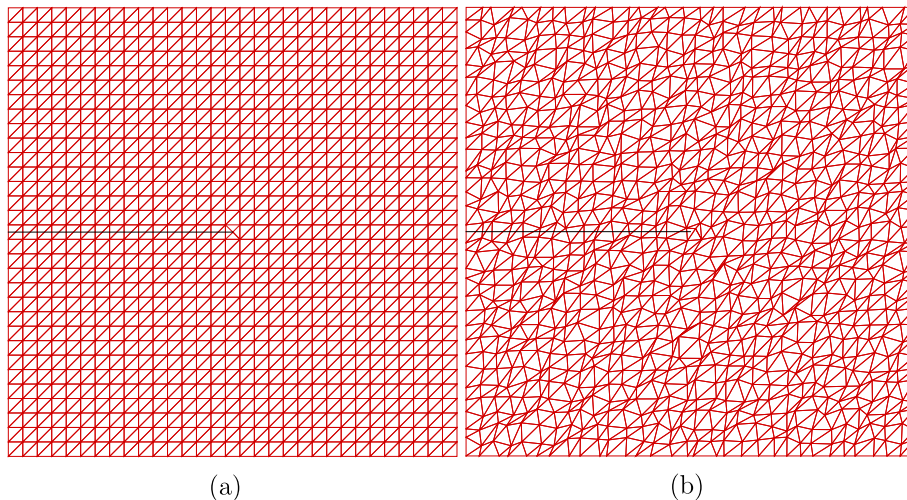
Fig. 18. Mesh design to check the mesh distortion effect: (a) structured mesh and (b) distorted mesh.

Fig. 19. Comparison of time costs for XFEM and XDFEM in Griffith crack problem.

Fig. 20. The comparison of the energy norm error in terms of (a) time and (b) DOFs.

Table 2
The error in the SIFs for the inclined center crack problem (47×47 structured mesh). XDFEM reduces the error by a factor of up to 2.0.

β	$K_I(\%)$		$K_{II}(\%)$	
	XFEM	XDFEM	XFEM	XDFEM
0	0.58	0.29	0.03	0.10
$\frac{\pi}{12}$	0.54	0.28	0.07	0.12
$\frac{\pi}{6}$	0.49	0.26	0.30	0.20
$\frac{\pi}{4}$	0.43	0.23	0.36	0.21
$\frac{\pi}{3}$	0.32	0.20	0.41	0.23
$\frac{5\pi}{12}$	$< 10^{-3}$	0.14	0.43	0.23
$\frac{\pi}{2}$	$< 10^{-3}$	$< 10^{-3}$	$< 10^{-3}$	$< 10^{-3}$

the increased cost associated with XDFEM is the increased bandwidth. This can be alleviated by using an 'element-by-element' approach.

4.2. Inclined center crack

An inclined crack problem is investigated in this section. The model is presented in Fig. 11(b). The infinite plate is subjected to remote tensile load in y direction and the inclination angle β is measured in the counter-clockwised direction from the x direction. The half crack length is $a = 5$. A square domain field (10×10) encircling the crack tip is selected and the exact displacement is applied on the boundary, as in the previous example. The analytical SIFs are given as

$$K_I = \sigma \sqrt{\pi a} \cos^2 \beta, \tag{41a}$$

$$K_{II} = \sigma \sqrt{\pi a} \cos \beta \sin \beta. \tag{41b}$$

Table 2 shows the relative error of K_I and K_{II} varying with the inclination angle of the crack. It can be observed from Table 2 that both XDFEM and XFEM results agree well with the analytical solu-

Fig. 21. Physical model of three points bending beam with three holes.

tion. The precision of the SIFs in the XDFEM are better than that of the XFEM. This example demonstrates that XDFEM performs well also for the mixed mode crack problems.

Table 3
Test cases for the three points bending beam problem.

	d	a	Crack increment	Number of propagation
Case 1	5	1.5	0.052	67
Case 2	6	1.0	0.060	69
Case 3	6	2.5	0.048	97

4.3. XDFEM for crack propagation

A three point bending beam with three holes is simulated in this section to test the versatility of XDFEM in simulating crack propagation. Holes strongly influence crack propagation in structures and the chosen example is a decisive test for computational fracture problems, as the crack path obtained is most sensitive to the accuracy of the crack driving force computation, as well as the chosen propagation increment, as will be seen below. This experiment is designed to explore the effect of holes on the crack trajectories. The geometry and load condition are illustrated in
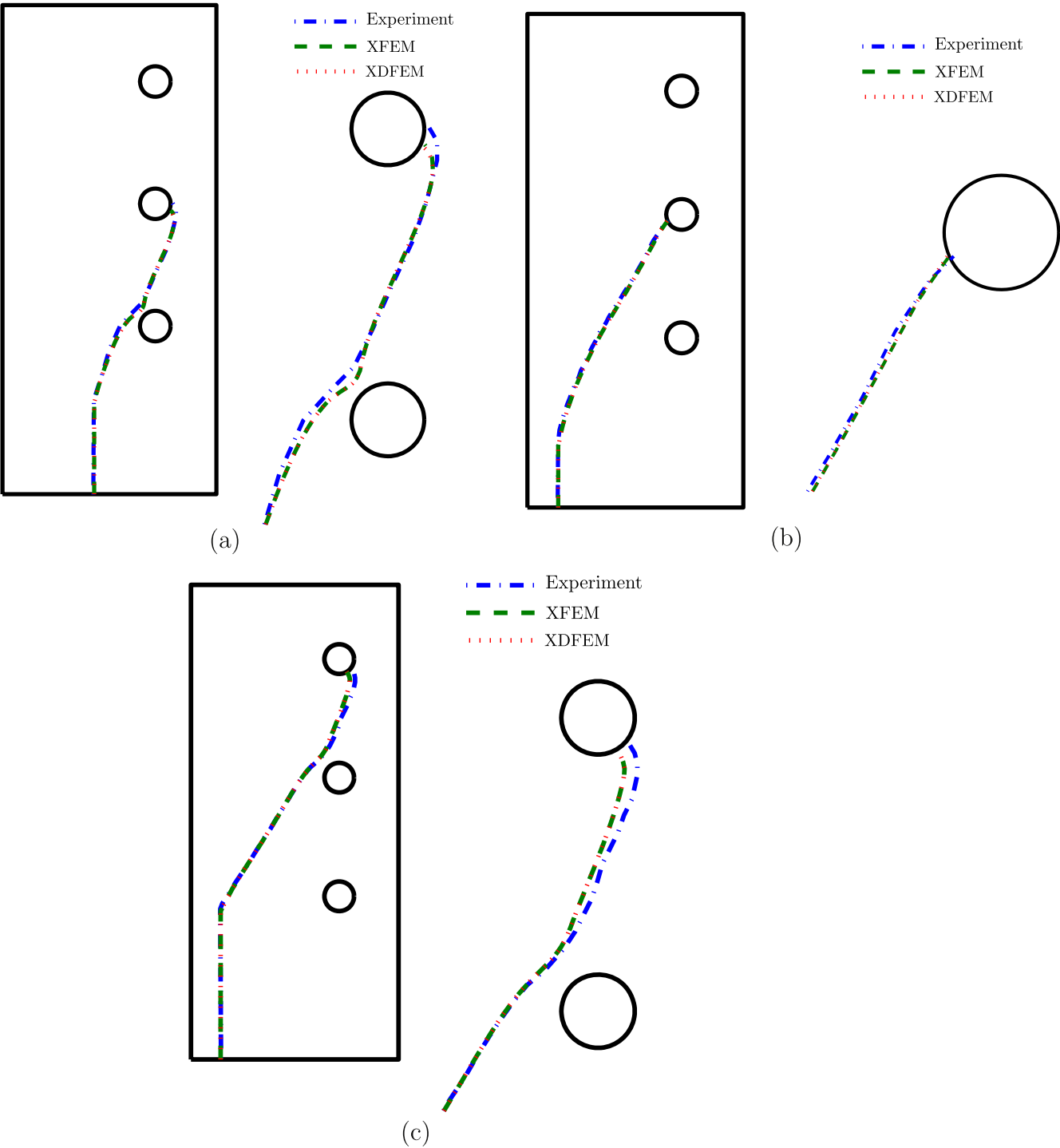
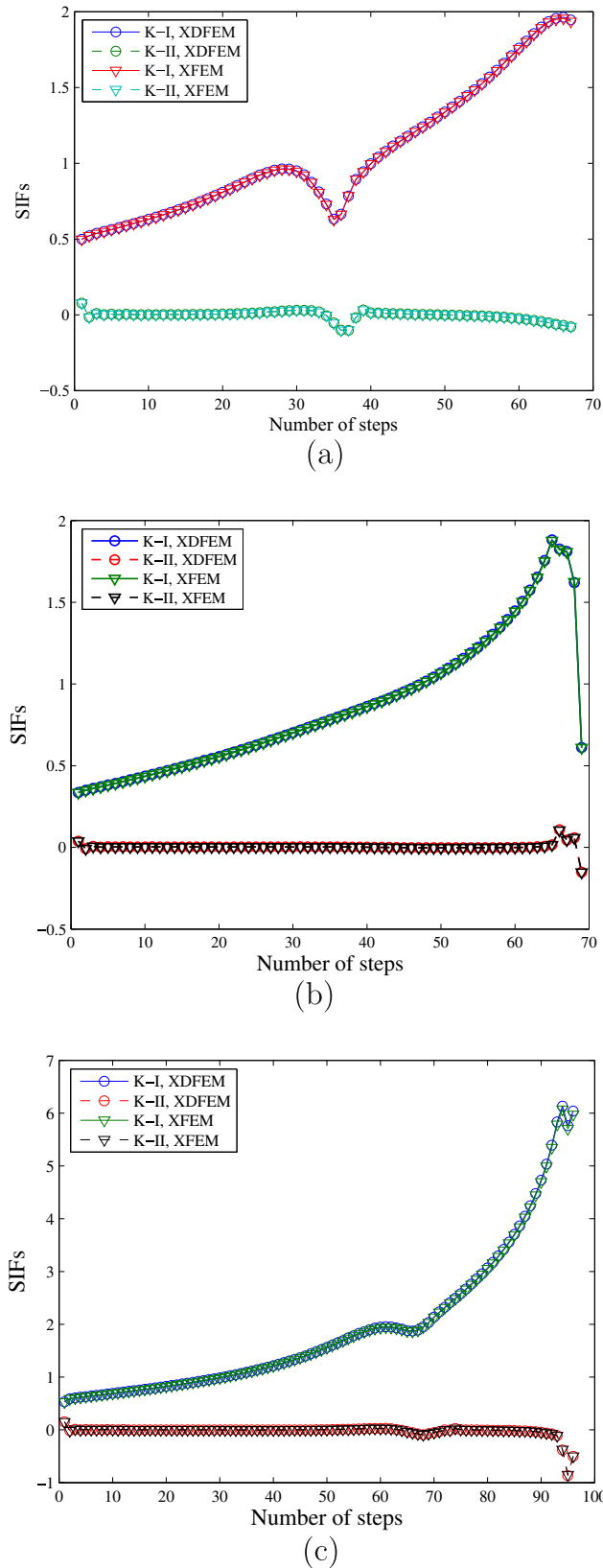**Fig. 22.** Crack evolution of the three cases.

(a)

(b)

(c)

Fig. 23. SIFs variation in three cases.

Fig. 21. Plexiglas specimens are used for which $E = 1000$ and $v = 0.37$ is used in the simulations. Plane strain condition is assumed. With the variation of the position of the initial crack,

different crack trajectories are obtained [38] [39]. A set of test cases, as listed in Table 3, are simulated. The maximum hoop stress criterion and the equivalent domain form of the interaction energy integral for SIFs extraction [1] is adopted to compute the orientation of crack propagation. The model is discretized by 27869 nodes and 55604 triangular elements. Fig. 22 illustrates the crack evolution of the listed three cases. And the results show that both methods are in good agreement with the experiment. In the numerical tests it is noted that, although the error in the energy norm lower in XDFEM, it can be observed from Fig. 22 that, there is very minor difference in the crack path trajectory between XFEM and XDFEM. However the crack paths obtained from both methods show a significant deviation when the crack passes the hole in case 1 and case 3. We should be aware that the different crack increment will affect the crack path as noticed in [40]. The SIFs for the three crack trajectories are plotted in Fig. 23. It can be observed that the SIFs tend to change in a bigger amplitude when the crack approaches the hole in case 1 and case 3. The XFEM and XDFEM SIFs for each case compare well. Fig. 24 compares the stress contours of the XFEM and the XDFEM. The XDFEM provides smooth stress fields without any post-processing.

5. Conclusions

This paper presented an enriched double-interpolation approximation method for linear elastic fracture and crack growth analysis. The double-interpolation approximation is constructed through two consequent stages of interpolation, i.e., the linear finite element interpolation for the first stage to produce an initial approximation field which will be utilized to reproduce the solution via a second interpolation with smooth nodal gradients. Several examples are tackled to explore the basic features of XDFEM. The key points are summarized as follows:

- The precision of the solution field is almost improved by one order of magnitude in both displacement and energy norm without increasing the total DOFs compared to linear FEs, due to the fact that the basis functions of the double-interpolation approximation have been enhanced through the embedment of area weighted 'average' gradients. DFEM proves to achieve higher accuracy based on simplex meshes and provide a practical and efficient modeling technique.
- The convergence rate of the DFEM is shown to behave midway between linear finite elements and quadratic finite elements. DFEM is more accurate than linear triangular Lagrange interpolants, less accurate than quadratic triangular elements, and offers a compromise between these two element classes. In contrast to common higher-order finite element, DFEM also provides C^1 continuity on most nodes. For continuum mechanics problems, it does not require any post-processing for recovering the nodal stresses. For fracture analysis, only the Heaviside and topological enriched nodes require extra post-processing. Post-processing procedure is thus unnecessary in DFEM and XDFEM, which improves the efficiency of the simulation and ensures all fields in the same space.
- It should be highlighted that the major factor which hampers the efficiency of DFEM is the increased bandwidth issue which is caused by the introduction of the average gradients. When the element-by-element strategy is used, this extra time needed in searching the stiffness matrix because of the expanded bandwidth can however be saved.
- The XDFEM provides a robust solution to crack propagation problems analogous to XFEM, whilst providing a smoother stress field without post-processing.
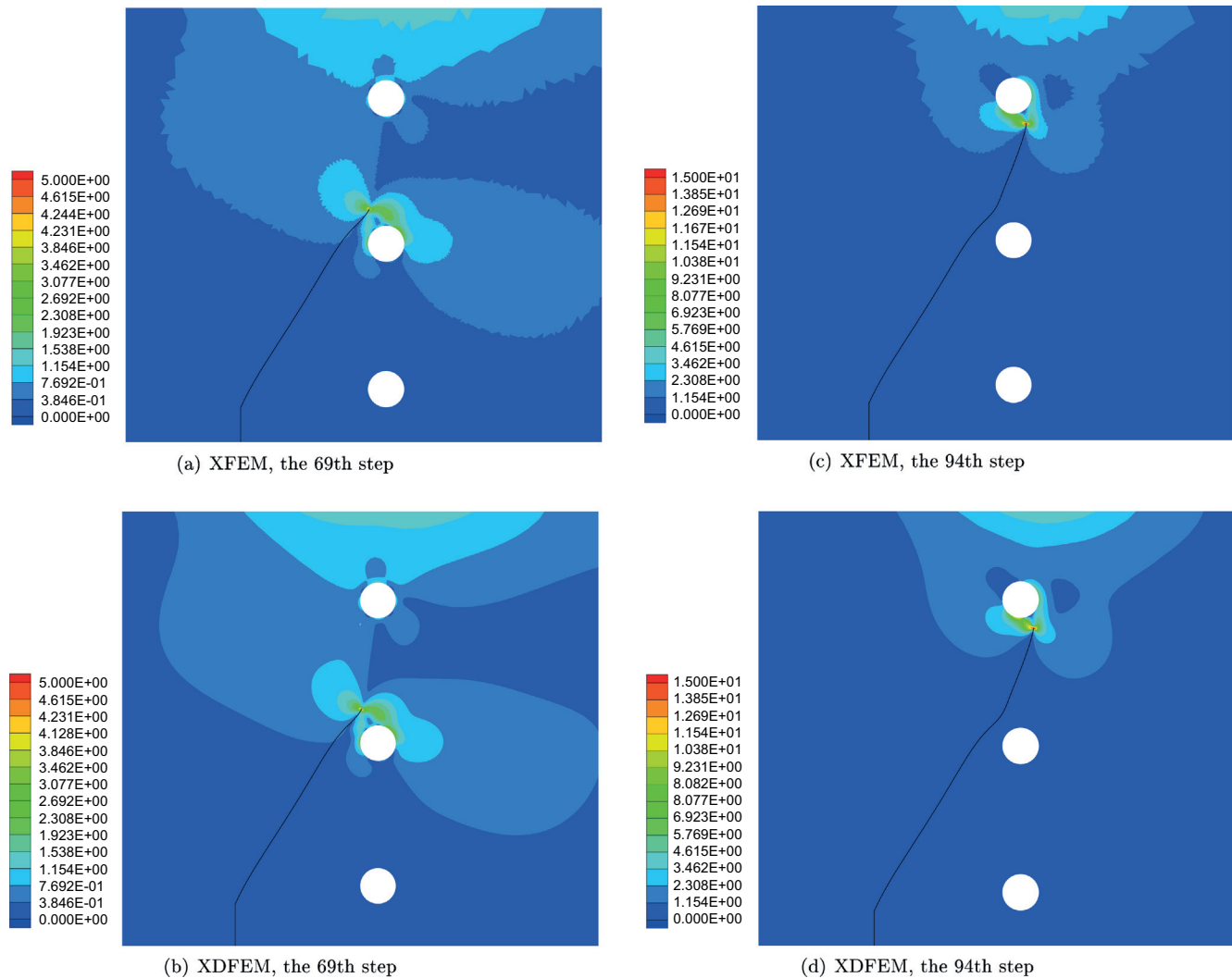
(a) XFEM, the 69th step

(c) XFEM, the 94th step

(b) XDFEM, the 69th step

(d) XDFEM, the 94th step

Fig. 24. Contour plots of Von Mises stress in case 3.

In future work, we plan on deriving and implementing the 3D XDFEM for fracture problems. Zienkiewicz-Zhu error estimation [41] based on XDFEM is also an interesting topic for investigation. Further it would be beneficial to identify a procedure to maintain C^1 continuity at the degenerated nodes.

References

[1] Moës N, Dolbow J, Belytschko T. A finite element method for crack growth without remeshing. Int J Numer Meth Eng 1999;46(1):131–50.

[2] Melenk JM, Babuška I. The partition of unity finite element method: basic theory and applications. Comput Methods Appl Mech Eng 1996;139(1–4):289–314.

[3] Strouboulis T, Copps K, Babuška I. The generalized finite element method. Comput Methods Appl Mech Eng 2001;190(32):4081–193.

[4] Fleck NA, Hutchinson JW. Strain gradient plasticity. Adv Appl Mech 1997;33(C):295–361.

[5] Krysl P, Belytschko T. Analysis of thin shells by the Element-Free Galerkin method. Int J Solids Struct 1996;33(20–22):3057–80.

[6] Fischer P, Mergheim J, Steinmann P. On the C1 continuous discretization of non-linear gradient elasticity: a comparison of NEM and FEM based on Bernstein-Bézier patches. Int J Numer Meth Eng 2010;82(10):1282–307.

[7] Papanicolopulos SA, Zervos A. A method for creating a class of triangular C 1 finite elements. Int J Numer Meth Eng 2012;89(11):1437–50.

[8] Papanicolopulos SA, Zervos A. Polynomial C1 shape functions on the triangle. Comput Struct 2013;118(0):53–8.

[9] Belytschko T, Lu YY, Gu L. Element-free Galerkin methods. Int J Numer Meth Eng 1994;37(2):229–56.

[10] Liu WK, Jun S, Zhang YF. Reproducing kernel particle methods. Int J Numer Meth Fluids 1995;20(8-9):1081–106.

[11] Davydov O, Sestini A, Morandi R. Local RBF approximation for scattered data fitting with bivariate splines. In: Mache DetlefH, Szabados József, Bruin MarcelG, editors. Trends and applications in constructive approximation. ISNM international series of numerical mathematics, vol. 151. Birkhäuser Basel; 2005. p. 91–102.

[12] Bordas SPA, Rabczuk T, Zi G. Three-dimensional crack initiation, propagation, branching and junction in non-linear materials by an extended meshfree method without asymptotic enrichment. Eng Fract Mech 2008;75(5):943–60.

[13] Zhuang X, Augarde C, Bordas S. Accurate fracture modelling using meshless methods, the visibility criterion and level sets: formulation and 2D modelling. Int J Numer Meth Eng 2011;86(2):249–68.

[14] Zhuang X, Augarde CE, Mathisen KM. Fracture modeling using meshless methods and level sets in 3D: framework and modeling. Int J Numer Meth Eng 2012;92(11):969–98.

[15] Zhuang X, Cai Y, Augarde C. A meshless sub-region radial point interpolation method for accurate calculation of crack tip fields. Theoret Appl Fract Mech 2014;69:118–25.

[16] Rabczuk T, Belytschko T. A three-dimensional large deformation meshfree method for arbitrary evolving cracks. Comput Methods Appl Mech Eng 2007;196(29):2777–99.

[17] Rabczuk T, Belytschko T. Cracking particles: a simplified meshfree method for arbitrary evolving cracks. Int J Numer Meth Eng 2004;61(13):2316–43.

[18] Chen L, Rabczuk T, Bordas SPA, Liu GR, Zeng KY, Kerfriden P. Extended finite element method with edge-based strain smoothing (ESm-XFEM) for linear elastic crack growth. Comput Methods Appl Mech Eng 2012;209–212:250–65.

[19] Bordas SPA, Rabczuk T, Nguyen-Xuan H, Nguyen VP, Natarajan S, Bog T, Quan DM, Hiep NV. Strain smoothing in FEM and XFEM. Comput. Struct. 2010;88(23–24):1419–43.

[20] Liu GR, Chen L, Nguyen-Thoi T, Zeng KY, Zhang GY. A novel singular node-based smoothed finite element method (NS-FEM) for upper bound solutions of fracture problems. Int J Numer Meth Eng 2010;83(11):1466–97.

[21] Vu-Bac N, Nguyen-Xuan H, Chen L, Bordas S, Kerfriden P, Simpson RN, et al. A Node-Based Smoothed eXtended Finite Element Method (NS-XFEM) for fracture analysis. Comput Model Eng Sci 2011;73(4):331–56.

[22] Bordas SPA, Natarajan S. On the performance of strain smoothing for quadratic and enriched finite element approximations (XFEM/GFEM/PUFEM). Int J Numer Meth Eng 2011;86(4–5):637–66.

[23] Zheng C, Wu SC, Tang XH, Zhang JH. A novel twice-interpolation finite element method for solid mechanics problems. Acta Mech Sin 2009;26(2):265–78.

[24] Wu SC, Zhang WH, Peng X, Miao BR. A twice-interpolation finite element method (TFEM) for crack propagation problems. Int J Comput Methods 2012;09(04):1250055.

[25] Duflot M, Bordas SPA. A posteriori error estimation for extended finite elements by an extended global recovery. Int J Numer Meth Eng 2008;76(8):1123–38.

[26] Bordas SPA, Duflot M. Derivative recovery and a posteriori error estimate for extended finite elements. Comput Methods Appl Mech Eng 2007;196(35-36):3381–99.

[27] Chessa J, Wang H, Belytschko T. On the construction of blending elements for local partition of unity enriched finite elements. Int J Numer Meth Eng 2003;57(7):1015–38.

[28] Gracie R, Wang H, Belytschko T. Blending in the extended finite element method by discontinuous Galerkin and assumed strain methods. Int J Numer Meth Eng 2008;74(11):1645–69.

[29] Fries T. A corrected XFEM approximation without problems in blending elements. Int J Numer Meth Eng 2008;75(5):503–32.

[30] Ventura G, Gracie R, Belytschko T. Fast integration and weight function blending in the extended finite element method. Int J Numer Meth Eng 2009;77(1):1–29.

[31] Ventura G. On the elimination of quadrature subcells for discontinuous functions in the eXtended Finite-Element Method. Int J Numer Meth Eng 2006;66(5):761–95.

[32] Natarajan S, Mahapatra DR, Bordas SPA. Integrating strong and weak discontinuities without integration subcells and example applications in an XFEM/GFEM framework. Int J Numer Meth Eng 2010;83(3):269–94.

[33] Laborde P, Pommier J, Renard Y, Salaün M. High-order extended finite element method for cracked domains. Int J Numer Meth Eng 2005;64(3):354–81.

[34] Bordas S, Nguyen PV, Dunant C, Guidoum A, Nguyen-Dang H. An extended finite element library. Int J Numer Meth Eng 2007;71(6):703–32.

[35] Westergaard HM. Bearing pressures and cracks. J Appl Mech 1939;6:A49–53.

[36] Béchet E, Minnebo H, Moës N, Burgardt B. Improved implementation and robustness study of the X-FEM for stress analysis around cracks. Int J Numer Meth Eng 2005;64(8):1033–56.

[37] Menk A, Bordas SPA. A robust preconditioning technique for the extended finite element method. Int J Numer Meth Eng 2011;85(13):1609–32.

[38] Ingraffea AR, Grigoriu M. Probabilistic fracture mechanics: a validation of predictive capability. Department of Structure Engineering, Cornell University; 1990. Rep. 90-8.

[39] Bittencourt TN, Wawrzynek PA, Ingraffea AR, Sousa JL. Quasi-automatic simulation of crack propagation for 2D LEFM problems. Eng Fract Mech 1996;55(2):321–34.

[40] Ventura G, Xu JX, Belytschko T. A vector level set method and new discontinuity approximations for crack growth by EFG. Int J Numer Meth Eng 2002;54(6):923–44.

[41] Zienkiewicz OC, Zhu JZ. The superconvergent patch recovery and a posteriori error estimates. Part 1: the recovery technique. Int J Numer Meth Eng 1992;33(7):1331–64.